

Tailoring P-N Conversion in All-solid-state Polymer Composites with A Record Ionic Thermopower

Cheng Chi

Tsinghua University

Meng An

Shaanxi University of Science and Technology

Xin Qi

Tsinghua University

Yang Li

The Hong Kong University of Science and Technology

Ruihan Zhang

Worcester Polytechnic Institute

Gongze Liu

The Hong Kong University of Science and Technology

He Huang

The Hong Kong University of Science and Technology

Hao Dang

Tsinghua University

Yan Wang

Worcester Polytechnic Institute

Weigang Ma (✉ maweigang@tsinghua.edu.cn)

Tsinghua University <https://orcid.org/0000-0003-0178-3994>

Baoling Huang

HKUST

Xing Zhang

Tsinghua University

Article

Keywords: polymer composites, ionic thermopower

Posted Date: January 7th, 2021

DOI: <https://doi.org/10.21203/rs.3.rs-130538/v1>

License:  This work is licensed under a Creative Commons Attribution 4.0 International License.

[Read Full License](#)

Version of Record: A version of this preprint was published at Nature Communications on January 11th, 2022. See the published version at <https://doi.org/10.1038/s41467-021-27885-2>.

1 Tailoring P-N Conversion in All-solid-state Polymer Composites with A Record 2 Ionic Thermopower

3 Cheng Chi^{1†}, Meng An^{1†}, Xin Qi¹, Yang Li², Ruihan Zhang³, Gongze Liu², He Huang², Hao Dang¹,
4 Yan Wang³, Weigang Ma^{1*}, Baoling Huang^{2*} and Xing Zhang¹

5 ¹ Key Laboratory for Thermal Science and Power Engineering of Ministry of Education, Department
6 of Engineering Mechanics, Tsinghua University, Beijing, 100084, China.

7 ² Department of Mechanical and Aerospace Engineering, The Hong Kong University of Science and
8 Technology, Clear Water Bay, Hong Kong SAR, China.

9 ³ Department of Mechanical Engineering, Worcester Polytechnic Institute, 100 Institute Road,
10 Worcester, MA 01609, USA.

11 *Corresponding author: W. G. Ma, email: maweigang@tsinghua.edu.cn; B. L. Huang, email:
12 mebhuang@ust.hk

13 † The authors contribute equally.

14

15 Abstract

16 All-solid-state organic polymer composites are promising ionic thermoelectric (*i*-TE) materials,
17 however, the transition from aqueous to organic gelation always sacrifices their thermoelectric
18 performance, especially the *n*-type thermopowers are severely unexplored, leaving the unrealized
19 large-scale application of *p-n* integrated *i*-TE devices. Herein, we successfully developed all-solid-
20 state PVDF-HFP/NaTFSI/PC (PhNP) with ultrahigh thermopower (S_i) of +20 mV K⁻¹. The
21 experimental and molecular simulation results detailly specified the relationship between the
22 interactions among ions and polymers and the highly enhanced thermopower. Meanwhile, a major
23 scientific breakthrough in *p-n* conversion from +20 to -6 mV K⁻¹ was achieved by incorporating
24 tris(pentafluorophenyl)borane (TPFPB) to capture Na⁺ and TFSI⁻ anions dominating the
25 thermodiffusion process. As a result, an all-solid-state *i*-TE generator generated a high voltage over
26 2.6 V at $\Delta T=10$ K and exhibited excellent cyclic stability under ambient air condition employing only

1 13 pairs of *p-n* couples, showing great potential for developing high-performance *i*-TE systems.

2 **Introduction**

3 Low-grade heat (<130°C) is abundantly available on earth, generating from various sources like
4 sun, geothermal and industrial plants^{1,2}. It was estimated that the generated low-grade heat from
5 geothermal is approximately over the annual energy demand of human activities³. However, most of
6 the low-grade heat is dissipated to the environment as waste heat, realizing heat recovery becomes one
7 of the most important missions around the world. Thermoelectric generators (TEGs) can directly
8 convert the temperature difference (heat) into electricity through the Seebeck effect. Although
9 inorganic semiconductors⁴ and semi-metals^{5,6} TE materials have been gained extensive exploration,
10 they still suffer from several obstacles, such as poor flexibility, substantial production cost, the
11 involving of toxic/scarce raw material and low thermopower ($\sim\mu\text{V K}^{-1}$), impeding them from large-
12 scale application⁷⁻⁹. Recently, high ionic thermopower or Seebeck coefficient (S_i) was found in the
13 ionic conducting polymer gels (PGs)^{8,10-13}, providing a new route to improve TE performance and
14 make TE technology more economically for future wide-scale application.

15 Theoretically, the temperature gradient (ΔT) motivated charge carriers (both cations and anions)
16 to migrate from the hot side to the cold side across the ionic thermoelectric (*i*-TE) materials, generating
17 an internal potential difference (ΔV_i) based on the Soret effect^{11,14-16}. Interestingly, aqueous ion-gels
18 were found to achieve a much higher thermopower than pure solutions^{7,15,17-20}. For example, PEO-
19 NaOH-H₂O¹⁵ exhibited a thermopower of 10 mV K⁻¹, cellulose-polystyrene sulfonate sodium (NFC-
20 PSSNa) had a thermopower of 8.4 mV K⁻¹ at 100% relative humidity (RH)²¹ and a synergistic KCl-
21 FeCN^{4-/3-} gelatin offered a high thermopower of 17.0 mV K⁻¹, which is much higher than pure
22 solutions of KCl (0.04 mV K⁻¹) and FeCN^{4-/3-} (1.4 mV K⁻¹)¹¹. But the aqueous ion-gels always need
23 to keep adequate moisture (high RH) and suppress the water evaporation from the gels otherwise their
24 performance could dramatically decay, at the same time they suffer from leakage, short operation time,

1 complex encapsulation problems²²⁻²⁴. Thus, all-solid-state materials are expected to develop next-
2 generation *i*-TE systems with durable performance. Several recent works have attempted to explore
3 the ionic thermoelectric properties of nonaqueous materials and obtained remarkable thermopower,
4 such as PVDF-HFP/EMIM:DCA (26 mV K⁻¹)⁷, polyaniline: polyelectrolyte (poly(2-acrylamido-2-
5 methyl-1-propane sulfonic acid): phytic acid (PANI:PAAMPSA:PA) (8.1 mV K⁻¹)⁹. It is conjectured that
6 the enhancement on thermopower is highly possible attributed to the formation of more interactions
7 between ions and polymer matrix and the improved structural entropy. However, the deep
8 understanding of the relationship of the formed interactions with ionic thermoelectric properties at the
9 atomic scale level is still not clear.

10 More importantly, the *i*-TE generators (*i*-TEGs) must connect *p*- and *n*-type thermocouples to
11 gain high performance, but most existing *i*-TE materials only have positive thermopowers, hampering
12 the widespread of *i*-TEGs^{8,10}. The *n*-type semiconductor materials could be easily obtained by doping
13 with electron donors, but such an approach cannot apply for *i*-TE materials since the ionic Seebeck
14 effect was generated by ions migration instead of electrons or holes. Accordingly, a scientific
15 breakthrough in tuning ionic thermopower is urgently needed. So far, few reports successfully
16 actualized *p-n* conversion in the liquid or all-solid-state *i*-TE systems. Jia et al.²⁵ intrigued the
17 thermopower conversion in water-[EMIm][Ac] binary liquid system with precise control over water
18 content (+2.4 to -0.98 mV K⁻¹). Duan et al.²⁶ incorporated poly (*N*-isopropylacrylamide) (PNIPAM) to
19 a liquid thermogalvanic cell to capture I₃⁻ at the hot side followed by the release of I₃⁻ at the cold side,
20 resulting in the thermopower of (I⁻/I₃⁻) redox couple changing from +0.71 to -1.91 mV K⁻¹. As known,
21 the thermopower of aqueous solutions is usually much inferior to solid-state polymer gel-based *i*-TE
22 systems. Research in the tuning the ionic thermopower of solid-state *i*-TE materials is more attractive⁸.
23 However, regulation ion thermodiffusion in all-solid-state polymer materials is much more complex
24 when the presence of polymer chains as they involve more interactions among ions and polymer chains.
25 Selectively control the diffusion of a specific charge type of ions without scarifying other properties

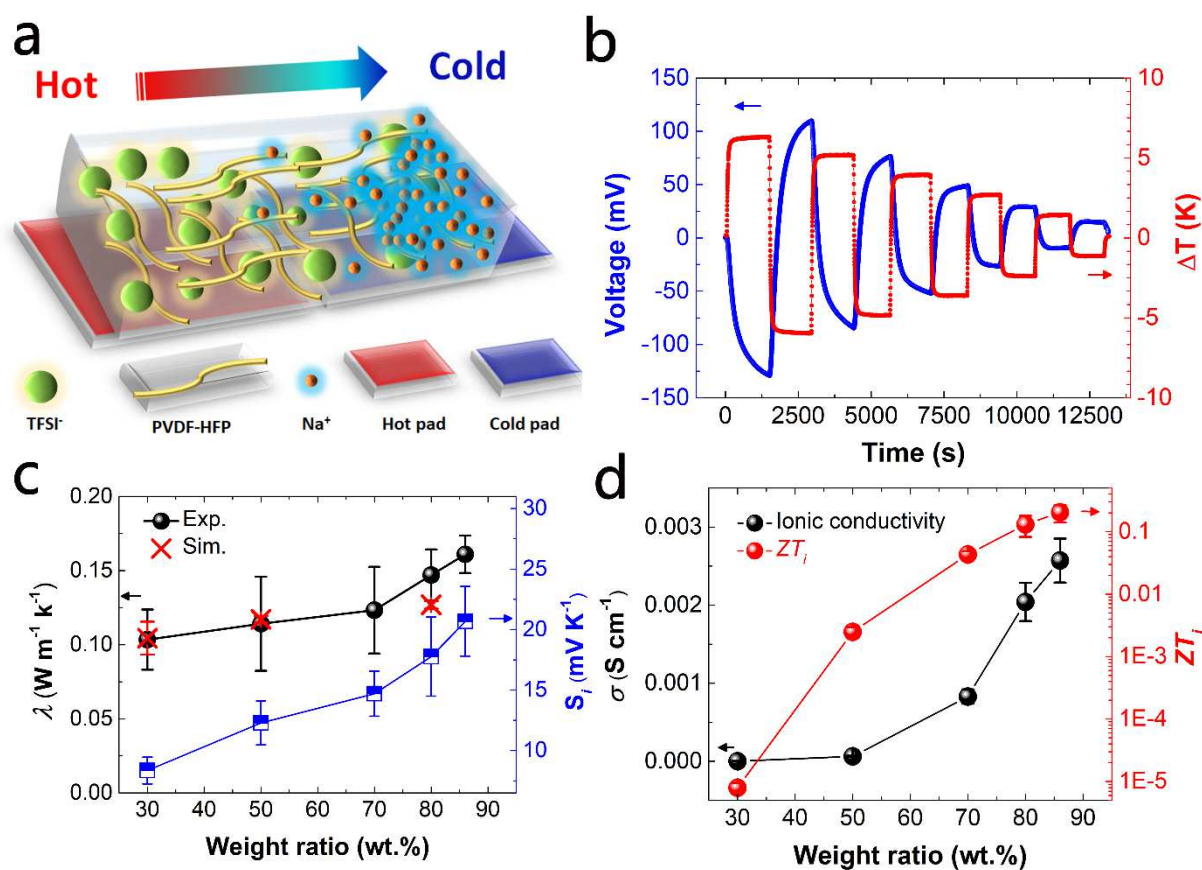
1 remained a big challenge. Thus, more efforts are needed to achieve to realize *p-n* conversion in all-
2 solid-state *i*-TE materials while maintaining high thermopower at the same time.

3 Here we report a strategy to overcome the above challenge by developing all-solid-state organic
4 *p-/n*-type ionic conducting PVDF-HFP/NaTFSI/PC (PhNP) composites exhibiting excellent
5 performance in the air. The *p*-type PhNPs delivered a high thermopower of 20 mV K⁻¹ by enhancing
6 structural entropy and enlarging thermal mass diffusion difference between cations Na⁺ and anions
7 TFSI⁻. Moreover, the *p*-type PhNP was successfully converted into *n*-type (-6 mV K⁻¹) by regulating
8 ions transportation. The Na⁺ cations were captured by the negative surface charged
9 tris(pentafluorophenyl)borane (TPFPB), making TFSI⁻ dominate the thermodiffusion process. To our
10 best knowledge, the developed all-solid-state organic *p-n* thermocouple exhibited the highest tuned
11 thermopower range till now. Finally, an all-solid-state ionic thermoelectric generator was fabricated
12 by 13 pairs of *p-n* thermocouples, obtaining over 2.6 V with $\Delta T=10\text{K}$ and outstanding stability without
13 any degradation after 50-cycle heat on-off operations in the air.

14 **Results**

15 **Thermoelectric properties of *p*-type PhNPs.** The developed organic *p*-type ionic conducting
16 composites are composed of PVDF-HFP and different weight percentages of NaTFSI/PC (1M),
17 ranging from 30 to 86wt.%, which were assigned as PhNP-30 to PhNP-86, respectively. The ionic
18 thermopower is one of the most crucial parameters for *i*-TE materials and is measured through a home-
19 made in-plane setup (Supplementary Fig. S1) which was calibrated with the reported materials in the
20 previous reports^{7,8,15}. To be noticed, the starting hot and cool ends of PhNPs were electrically connected
21 to the positive and negative poles of a voltmeter, respectively. When a temperature difference ($\Delta T=+6$
22 K, red line, Fig. 1b) was applied, a negative thermal potential of PhNP-86 was produced (blue line,
23 Fig. 1b). Once alternating of the hot and cool side ($\Delta T=-6$ K), the generated thermoelectric voltage
24 instantly turned to the positive direction correspondingly (Fig. 1b), demonstrating rapid and reversible

1 thermal response behavior. The observations suggested a higher concentration of positive Na^+ cations
 2 accumulated at the cool side as illustrated in Fig. 1a. It implied the thermal mobility of Na^+ ions was
 3 larger than that of TFSI^- anions, belonging to a p -type i -TE material^{8,11}. Besides, the higher the
 4 temperature difference, the larger thermoelectric voltage was generated by PhNPs, exhibiting
 5 outstanding capability in thermal-intensity sensing. The S_i of each PhNPs was obtained by fitting the
 6 slope of the measured ΔV_i - ΔT curves (Supplementary Fig. S2). Interestingly, by introducing more
 7 amount of NaTFSI/PC, the thermopower of the PhNPs gradually increased and the highest value
 8 reached around $20 \pm 4 \text{ mV K}^{-1}$ of PhNP-86 (blue line, Fig. 1c) in the air with RH of 68%, demonstrating
 9 a very competitive performance over the recently reported works, such as 11 mV K^{-1} of
 10 PEO/NaOH/ H_2O ¹⁵ and 13 mV K^{-1} of PVDF-HFP/EMIMTFSI/PEG⁸.



11
 12 **Fig. 1: The thermoelectric performance of the p -type PhNP.** (a) The diagrammatic illustration of the p -type (Na^+ dominate thermodiffusion) PhNP i -
 13 TE materials. (b) The plot of the measured V_i - T curves of PhNP-86. (c) The measured thermopower, thermal conductivity together with simulation results
 14 of PhNPs. (d) The measured ionic conductivity and figure of merit ZT_i of each PhNPs.

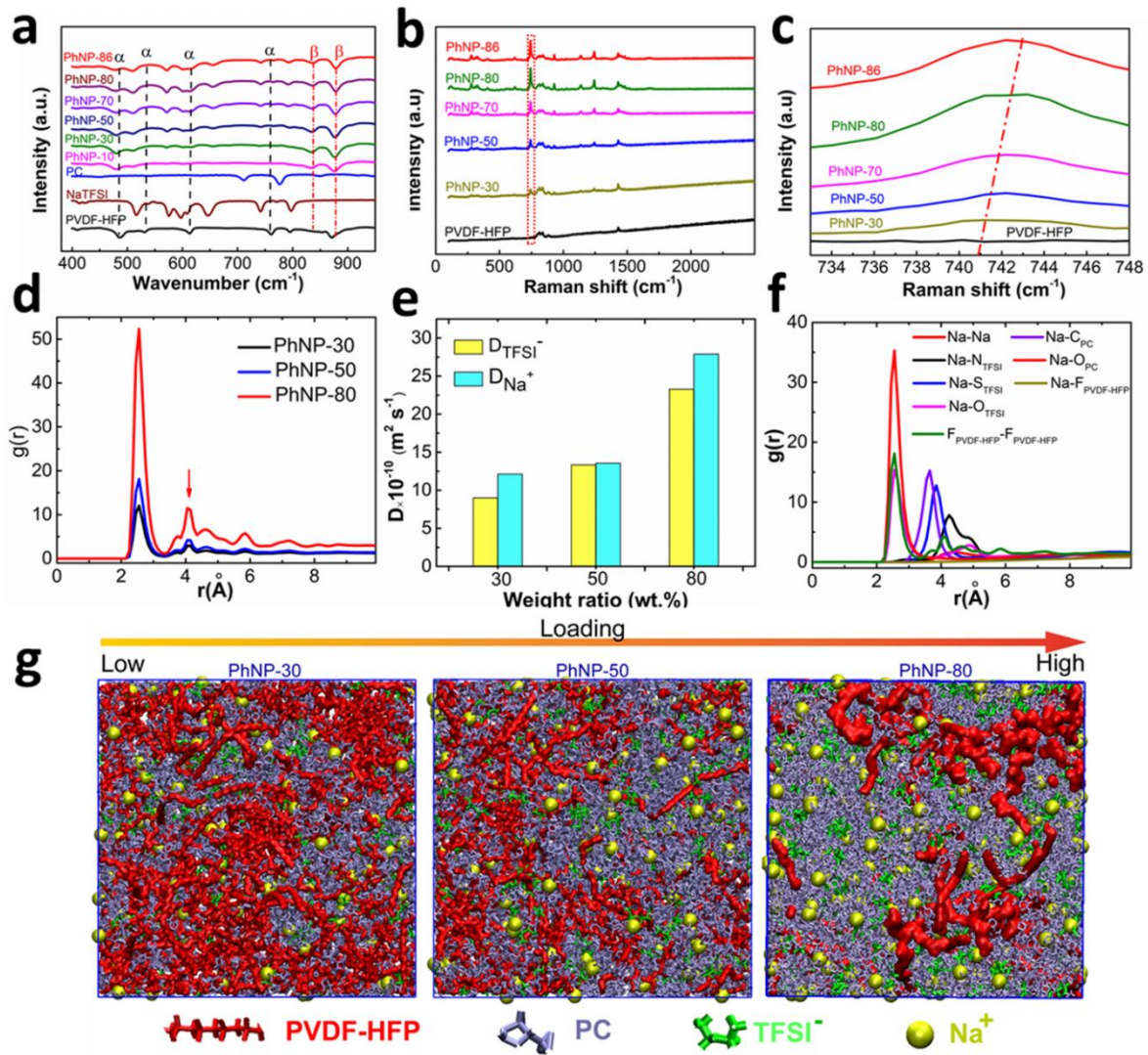
1 **Thermopower analysis.** Obviously, the thermopower of the developed PhNPs is significantly
2 influenced by the weight loading of NaTFSI/PC. As proposed in a very recent work by Liu et al.¹¹, the
3 generated thermopower can be described by Eq. (1):

$$4 \quad S_{td} = \frac{\sum_i q_i n_i^0 \hat{S}_i D_i}{\sum_i q_i^2 n_i^0 D_i}, \quad (1)$$

5 where q , n , i , \hat{S} and D represent charges, concentration, ion species, the Eastman entropy of transfer
6 and diffusion coefficient, respectively. S_{td} is strongly close to the change in structural entropy and mass
7 transport difference between positive and negative ions at a given temperature difference. Previous
8 works^{11,15,17} found the interaction between ions and polymer matrix was considered to have a
9 substantial impact on the structural entropy. To understand the interaction between PVDF-HFP and
10 NaTFSI/PC, the Fourier transform infrared spectroscopy (FTIR) characterization from 400-950 cm^{-1}
11 of each PhNPs was conducted, as shown in Fig. 2a. Upon incorporation of NaTFSI/PC into PVDF-
12 HFP, the intensity of the crystalline phase (α -phase) of PVDF-HFP, which located at 980 cm^{-1} ($-\text{CF}_2$
13 and $-\text{CC}$ symmetric stretching), 796 cm^{-1} ($-\text{CF}_3$ stretching), 762 cm^{-1} ($-\text{CH}_2$ rocking), 614 cm^{-1}
14 ($-\text{CF}_2$ bending and CCC skeletal), and 531 cm^{-1} ($-\text{CF}_2$ wagging)^{27,28}, gradually decreased and peaks
15 of 614 cm^{-1} and 762 cm^{-1} even disappeared at higher concentration of NaTFSI/PC. Meanwhile, the
16 peak at 879 cm^{-1} belonging to the amorphous phase (β -phase) became dominant and a new β -phase
17 peak at 841 cm^{-1} appeared. The confirmation of the new β -phase was attributed to the interaction
18 between the dipole moment of polymer and ions in which a large spontaneous polarization can be
19 generated.^{29,30} Thus, the new-formed ion-dipole interactions are believed to enhance structural entropy
20 during ions transport, leading to the enhancement of thermopower⁷.

21 To gain molecular-level insights into the ion transport and thermal properties, we performed all-
22 atom molecular dynamics (MD) simulations and the details of calculations are illustrated in
23 Supplementary materials part II. Figure 2g shows the simulation snapshots taken from the PhNP-30, -
24 50 and -80 samples, where the PVDF-HFP chains, PC small molecules, anions TFSI⁻ and cations Na⁺

1 distribute uniformly in the simulations cell. When increasing the mass loading of NaTFSI/PC, the
 2 intertwined chains of PVDF-HFP tend to spread and the interactions among chains/ions could be
 3 changed accordingly (Fig. 2g). The SEM also found that the packed PVDF-HFP was quickly changed
 4 to the porous structure of PhNPs and the size of quasi-spherical grains of the polymer chains gradually
 5 decreased, as shown in Supplementary Fig. S3a-1j, which are consistent with the built MD model in
 6 Fig. 2g. The calculated radial distribution functions (RDFs) from MD simulations between F atoms in



7
 8 **Fig. 2: The structural characterization and atomic-level interaction in PhNPs.**(a) FTIR spectra with a range of 400-950 cm^{-1} , (b) Raman spectra with
 9 a range of 100-2500 cm^{-1} , and (c) the enlarged view of Raman spectra with a range of 733-746 cm^{-1} of each PhNPs. (d) the calculated RDFs (e) and the
 10 diffusion coefficient of Na^+ and TFSI^- of the PhNP-30, -50 and -80 samples. (f) The RDF of each interaction among ions and PVDF-HFP of PhNP-50.
 11 (g) The snapshots of the MD simulation model.

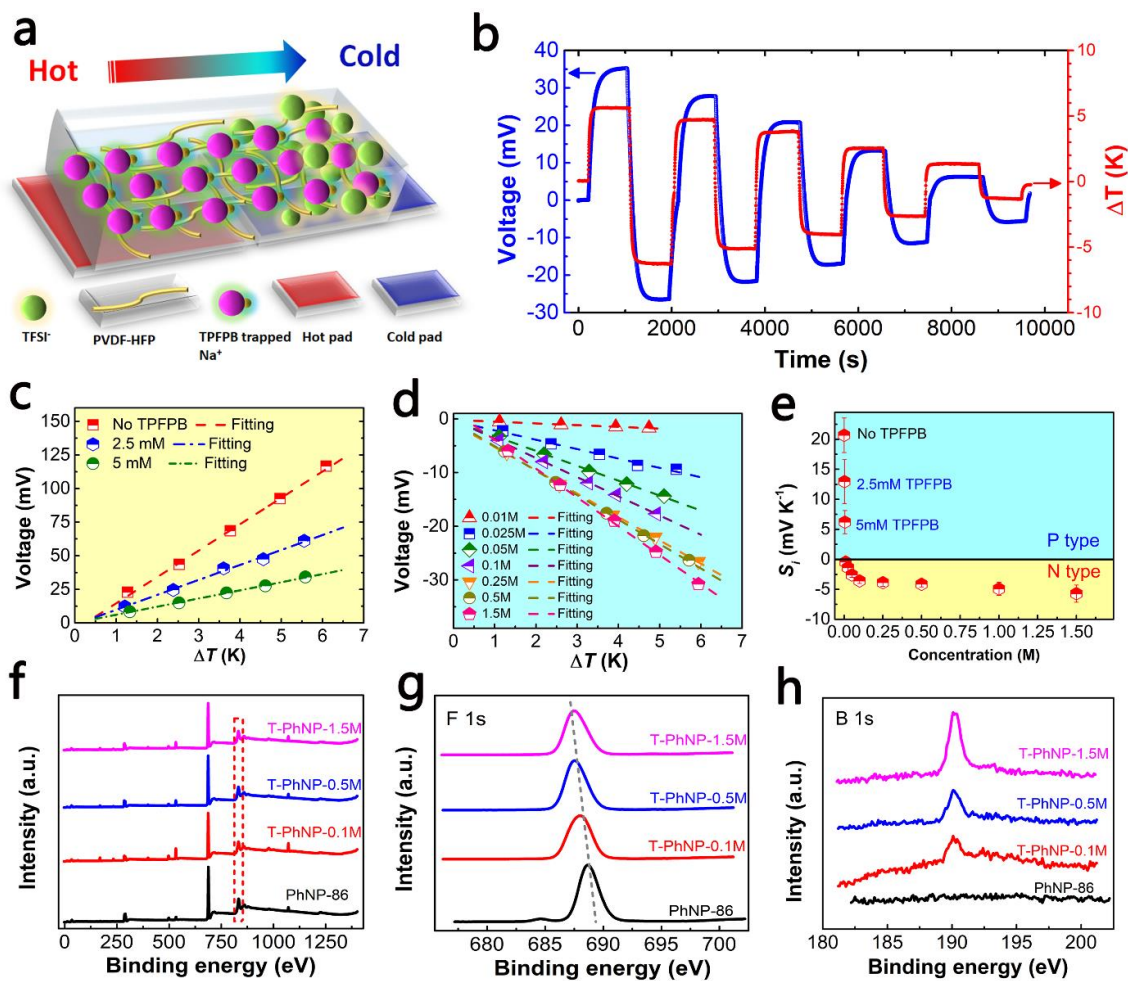
1 PVDF-HFP showed that the amplitude of the first peak at 2.5 Å increased from the sample PhNP-30
2 to PhNP-80 (Fig. 2d), indicating more structural heterogeneity in the high NaTFSI/PC loading system.
3 The RDF is defined as the probability of finding a pair of atoms at a particular separation compared to
4 that of a random distribution at the same density. It also suggests that the local density of the PVDF-
5 HFP chains in the PVDF-HFP domained area will be much higher than the average value over the
6 whole simulations and explain the large variation in peak height. Meanwhile, we also observed a new
7 peak at 4.2 Å gradually loomed with the increasing content of NaTFSI/PC. This new peak strongly
8 implies that partial interaction at 2.5 Å converts to weak force among PVDF-HFP separated chains in
9 PhNP-80. This is consistent with the emerging new phase in the experimental finding in Fig. 2a.
10 Meanwhile, the spread of chains enhanced the possibility to expose more PVDF-HFP functional sites
11 to ions, leading to more interactions with ions, which may be one of the physical mechanisms of
12 enhancing the structural entropy.

13 Another important factor to improve thermopower is attributed to enlarge mass transport
14 differences of cations and anions which usually can produce higher charge imbalance. From Raman
15 analysis in Fig. 2b, it is easy to find the intensity of the peak located at 741 cm^{-1} , which is assigned to
16 TFSI⁻, gradually becomes more predominant, confirming the high mass loading of NaTFSI/PC.
17 Meanwhile, the peak position of TFSI⁻ exhibited a shift to larger wavelength or low energy direction
18 (Fig. 2c), which indicates that more amount of the dissociated TFSI⁻ anions formed contact ion pairs
19 due to larger ion volume³¹. The formed contact ion clusters could impede the transport of TFSI⁻, which
20 might be responsible for enlarging the mass transport difference between Na⁺ and TFSI⁻. The
21 computational analysis had shown that the diffusion coefficient of Na⁺ cations ($2.79 \times 10^{-9} \text{ m}^2 \text{ s}^{-1}$) is
22 substantially higher than that of TFSI⁻ anions ($2.32 \times 10^{-9} \text{ m}^2 \text{ s}^{-1}$) of PhNP-80 (Fig. 2e). As the
23 counterion condensation limiting laws proposed by Manning³², a small portion of cations incline to
24 condensate along the negative sites of polymer chains. These condensed Na⁺ around the PVDF-HFP
25 chains could induce frictional drags on TFSI⁻, which impeded the transportation of TFSI⁻. The remained

1 free Na⁺ gained higher mobility than those of TFSI⁻ dragged by the condensed Na⁺ cations¹¹, favoring
2 to obtain higher thermoelectric voltage arising from charges imbalance.

3 **Ionic and thermal conductivity analysis.** The ionic conductivity (σ_i) of each PhNPs was measured
4 by the electrochemical impedance method³³ and the corresponding measured impedance spectra were
5 plotted in Supplementary Fig. S4. Clearly, the ionic conductivity was also dramatically improved from
6 the PhNP-30 of $\sim 4 \times 10^{-7}$ S cm⁻¹ to the highest value in PhNP-86 of $\sim 2.6 \times 10^{-3}$ S cm⁻¹ (Fig. 1d) which is
7 near to the pure liquid NaTFSI/PC (6×10^{-3} S cm⁻¹). At the high content of NaTFSI/PC, the PhNP-86
8 formed a relatively homogeneous and cross-linked porous structure as observed from the cross-section
9 view in Supplementary Fig. S3f, which can significantly improve the diffusion coefficient of ions (Fig.
10 2e) and facilitate the ions transport^{34,35}. Also, the thermal conductivity (λ_i) of the PhNPs exhibited a
11 nearly rising trend from 0.1 to 0.16 W m⁻¹ K⁻¹ with the increasing loading content of NaTFSI/PC (Fig.
12 1c). The calculated thermal conductivities for PhNP-30, -50, -80 are around 0.1, 0.117 and 0.127 W
13 m⁻¹ K⁻¹, respectively, which matched well with experimental data (Fig. 1c) and were consistent with
14 the thermal conductivity range (0.1~0.3 W m⁻¹ K⁻¹) of amorphous materials^{36,37}. Besides, the increased
15 thermal conductivity of PhNPs was ascribed to the enhanced heat transport contribution from
16 electrostatic interactions between ions and the surrounding environment in the system with an
17 increasing amount of NaTFSI/PC. To better understand the interatomic interactions, the RDFs of Na-
18 O_{PC}, Na-O_{TFSI}, Na-N_{TFSI}, Na-S_{TFSI}, Na-C_{PC}, and F_{PVDF-HFP}-F_{PVDF-HFP} pairs of PhNP-50 as a typical
19 example were studied. Figure 2f showed that a peak position at around 2.6 Å between the charged
20 pairs (Na-Na, Na-O_{PC}, and Na-O_{TFSI}) which suggested the distance of the charged pairs is more likely
21 to be closer than the other pairs, i. e. Na-F_{PVDF-HFP}, Na-C_{PC}, and Na-S_{TFSI} pairs due to the stronger
22 electrostatic interactions among the former charged pairs. As the loading of NaTFSI/PC increasing,
23 they provided a larger of proportional electrostatic interactions and more thermal pathways for phonon
24 transport due to the transition from weak van der Waals interaction to strong Coulomb interactions.

1 Similar to semiconductor-based TE materials^{5,38}, the dimensionless ionic figure of merit ZT_i , which is
 2 defined as $ZT_i = S_i^2 \sigma_i T / \lambda_i$, is used to characterize the performance of *i*-TE materials¹⁴. The high
 3 thermopower and ionic conductivity and low thermal conductivity of the developed PhNPs greatly
 4 contribute to achieving a high ZT_i . As a result, the ZT_i of PhNP-86 reached over 0.2 at 298 K and 68%
 5 RH, as shown in Fig. 1d, which is significantly higher than some recently reported *i*-TE materials such
 6 as PEO-NaOH (0.014)¹⁵, PSSNa (0.013)³⁹ and PVDF-HFP/EMMI:TFSI (0.007)⁸ and close to the
 7 tetrachloro-perylene bisimide (4Cl-PBI) (0.23)⁴⁰, PVDF-HFP-EMIM:DCA (0.75)⁷.



8

9 **Fig. 3: The conversion in p-type PhNP to n-type T-PhNP.** (a) The schematic of ion transport of *n*-type (TFSI⁻ dominate thermodiffusion) T-PhNP *i*-TE
 10 materials. (b) The measured thermoelectric voltage at a series of temperature difference of T-PhNP-1.5M. (c) and (d) The plot of $\Delta V_T / \Delta T$ fitting curves
 11 and the calculated thermopower of each T-PhNPs. (f) XPS characterization of (g) F (1s) peak and (h) B (1s) peak of the T-PhNP with different amounts
 12 of TFPFB.

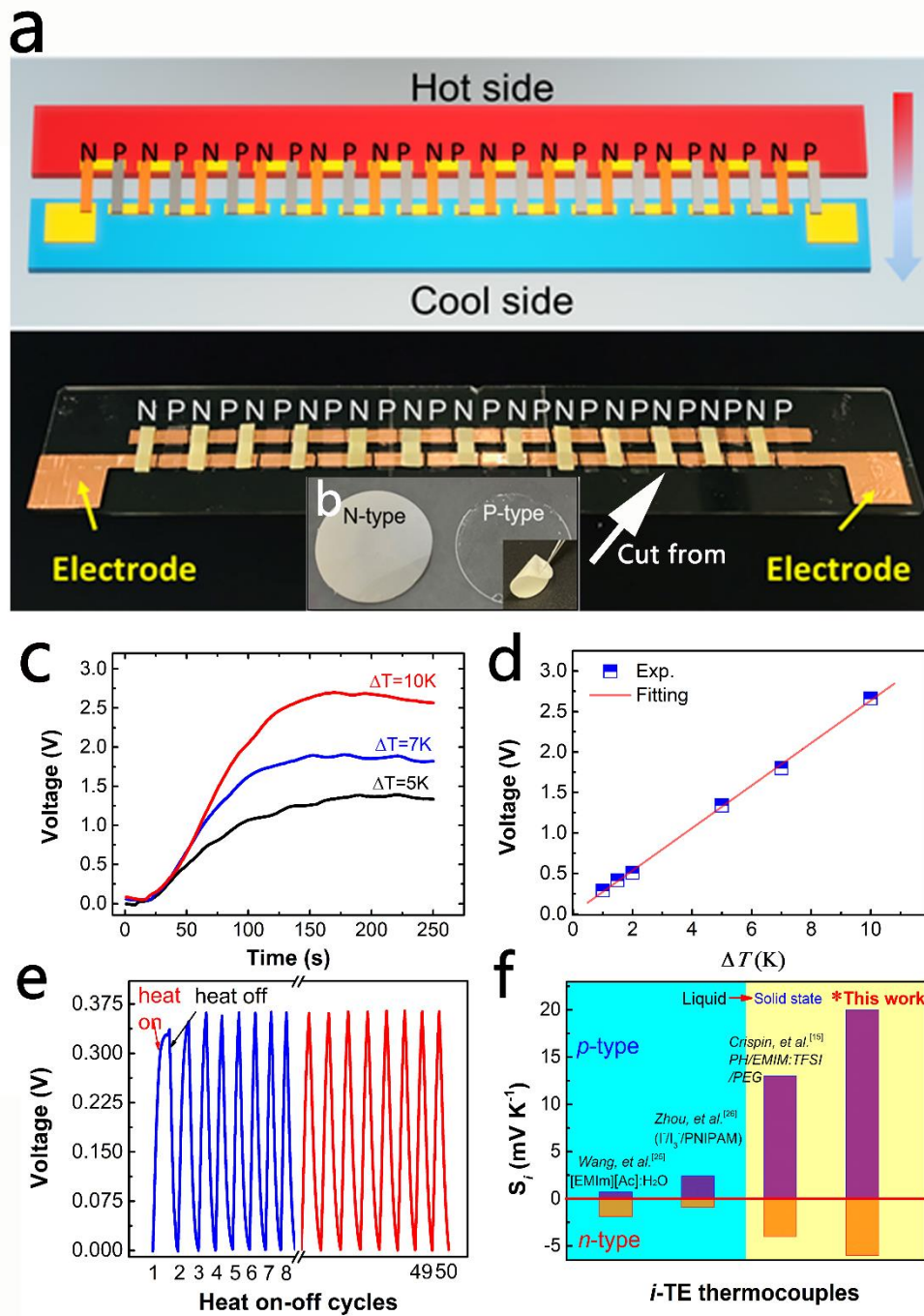
1 **Converting PhNP to n-type T-PhNP.** Selective tuning the sign of the thermopower is a significant
2 way to realize the *p-n* conversion in *i*-TE materials, which is essential to develop the module-type TE
3 generators. After introducing 1.5M TPFPB to PhNP-86, the thermopower of the new-formed
4 composite was measured under the same testing procedures as *p*-type PhNPs. The produced
5 thermoelectric voltage of PhNP-86 with 1.5M TPFPB sample exhibited a positive value (red line, Fig.
6 3b) under a ΔT (+6 K), which was clearly opposed to *p*-type PhNP-86. The revising sign of
7 thermoelectric voltage strongly revealed that a higher concentration of TFSI⁻ was generated at the cool
8 side (Fig. 3a), indicating TFSI⁻ anions dominated the thermodiffusion process, realizing *p-n* conversion
9 in the organic ionic conducting PhNPs. To comprehensively study the influence of TPFPB on tuning
10 thermopower, the incorporation with different concentrations of TPFPB was investigated. A series of
11 concentrations of TPFPB from 2.5 mM to 1.5 M were introduced into the developed *p*-type PhNP-86,
12 forming new ion-gels and were assigned as T-PhNP-*x*M, where *x* denoted the concentration of TPFPB.
13 The original porous morphologies of T-PhNPs gradually became more dense structures and the pores
14 were even fulfilled at higher concentrations of the TPFPB (Supplementary Fig. S5a-5c). The EDS
15 mapping of T-PhNP-0.5M (Supplementary Fig. S5d) demonstrated the distribution of each element of
16 the fabricated *i*-TE materials. Specifically, the boron (B) element only coming from TPFPB was found
17 on the surface of T-PhNPs, confirming that the new T-PhNPs composites were successfully formed.

18 Interestingly, the slope of the fitted ΔV_i - ΔT curves of T-PhNP-2.5mM and T-PhNP-5mM
19 gradually decreased and thermopower of the T-PhNPs decreased to 12.95 and 6.2 mV K⁻¹, respectively.
20 It indicated the thermodiffusion of cations was impeded as shown in Fig. 3c. And the slope of ΔV_i - ΔT
21 curves and the thermopower reached almost zero of T-PhNPs-0.01M (Fig. 3d), implying the
22 thermodiffusion of cations is nearly close to anions. Moreover, when the concentration of TPFPB
23 exceeded this critical point, the thermopower became more negative with containing more amount of
24 TPFPB (Fig. 3d-3e and Supplementary Fig. S6), strongly suggesting the thermodiffusion of anions
25 was easier than cations of the new T-PhNPs. And the maximum value reached around -6 ± 1 mV K⁻¹ of

1 T-PhNP-1.5M, which is higher than those of the reported organic *n*-type *i*-TE materials so far, such as
2 the PVDF-HFP/EMIMTFSI (-4 mV K^{-1})⁸, 4Cl-PBI (-3.02 mV K^{-1})⁴⁰ at room temperature. Here, the
3 TPFPB molecular has 15 F atoms, forming a negative-charged enriched environment in the composite,
4 which could trap Na^+ ions and thus hindering their transport, in turn making TFSI⁻ anions dominate
5 the thermodiffusion process. From the X-ray photoelectron spectroscopy (XPS) analysis (Fig. 3f-3g),
6 it is clear to find the binding energy of F1s tends to shift from 688 eV to 686 eV upon adding TPFPB.
7 Since the interaction between F and Na^+ could change the energy status of F of TPFPB, making the
8 binding energy towards the Na-F of which the binding energy is around 684 eV⁴¹. The intensity of the
9 peak located at 191 eV (Fig. 3h), which is assigned to B, became stronger due to the increasing
10 concentration of TPFPB.

11 **The prototype of all-solid-state *i*-TEGs.** Both developed *p*-type PhNP (transparent) and *n*-type T-
12 PhNP (light yellow) exhibited solid status as well as excellent flexibility (Fig. 4a), which is significant
13 for developing all-solid-state high-performance *i*-TEGs. An in-plane *i*-TEG module including 13 pairs
14 thermocouples of *p*-type PhNP-86 and *n*-type T-PhNP-1.5M films was designed and fabricated shown
15 in Fig. 4b. The ionic TE performance of the fabricated *i*-TEG module was investigated under various
16 ΔT from 1 to 10 K in the air. The produced thermoelectric voltage of the *i*-TEG module reached almost
17 $\sim 2.6 \text{ V}$ at $\Delta T=10 \text{ K}$ in less than 200s (Fig. 4c), indicating fast ionic thermal response property.
18 Moreover, the overall thermopower of this *i*-TEG module reached as high as 0.263 V K^{-1} (Fig. 4d),
19 which is near to the theoretical sum of the thermopower of PhNP-86 and T-PhNP-1.5M thermocouples
20 (0.338 V K^{-1}). To our best knowledge, the developed PhNP/T-PhNP thermocouple demonstrated the
21 highest thermopower tuned range compared to the recent reported *i*-TE thermocouples up to the
22 present, such as PVDF-HFP/EMIM:TFSI/PEG (-4 to 13 mV K^{-1})⁸, $\text{H}_2\text{O}/\text{EMIM}:\text{AC}$ (2.41 to -0.92 mV
23 K^{-1})²⁵ and $\text{I}^-/\text{I}_3^-/\text{PNIPAM}$ (0.71 to -1.91 mV K^{-1})²⁶ ion-gels, as summarized in Fig. 4f. Meanwhile, the
24 reproducible stability of the *i*-TEGs was also investigated in an ambient condition which is very
25 significant for the practical application. After the repeating heating-cooling test in the air, the produced

1 thermoelectric voltage of the fabricated *i*-TEG demonstrated no obvious decay and exhibited nearly
 2 ideal repeatability even after 50 cycles, indicating excellent stability (Fig. 4e). Overall, the fabricated
 3 *i*-TEG module platform holds the promising potential of application in low-grade heat harvesting,
 4 flexible power sources and heat sensing.



5
 6 Fig.4: The performance of the prototype of all-solid-state *i*-TEGs. (a) The digital photo of design and fabricated in-plane *i*-TEG with 13 pairs of *p*-*n*

1 thermocouples and (b) inset: the fabricated free-standing all-solid-state T-PhNP-1.5M (left) and PhNP-86 (right) film. (c) The thermoelectric voltage (V)
2 vs time (t) curves and (d) the V - t fitting curves of the fabricated i -TEG under various ΔT . (e) The 50-cycles heat on/off stability test of the as-fabricated
3 i -TEG under 1.5 K. (f) Comparison of the thermopower range for the recent reported i -TE materials realizing p - n conversion^{8,25,26}.

4 **Discussion**

5 In conclusion, this work developed a pair of all-solid-state p - (PhNP-86) and n -type (T-PhNP-1.5M) i -
6 TE material with the largest thermopower range ($-6 \sim 20$ mV K⁻¹) at room temperature for the first
7 time. The strong interaction between ions and dipoles of the PVDF-HFP matrix significantly enhanced
8 the structural entropy, combining the enlarged mass transport difference between Na⁺ and TFSI⁻ at
9 higher mass content, attributing to outstanding thermopower properties. Moreover, the p - n conversion
10 was successfully achieved through a facial way by introducing a certain amount of TPFPB. The results
11 proved that the negative surface charged TPFPB impede Na⁺ ions transport and made TFSI⁻ dominate
12 the thermodiffusion process. Besides, an in-plane all-solid-state i -TEG prototype was made of 13 pairs
13 of p - n thermocouples, achieving ultra-high thermoelectric voltage of ~ 2.6 V at $\Delta T=10$ K and exhibiting
14 outstanding stability without any obvious degradation after 50-cycle heat on-off operation in the air.
15 This work developed a novel way to obtain high thermopower and simultaneously realized the p - n
16 conversion in the solid-state i -TE material, which is significantly beneficial for the development of
17 next-generation all-solid-state flexible i -TE systems.

18 **Methods**

19 **Materials.** Polyvinylidene fluoride-hexafluoropropylene pellet (PVDF-HFP, average M_w , 455,000 g
20 mol⁻¹), sodium bis(trifluoromethylsulfonyl)imide (NaTFSI), propylene carbonate (PC, anhydrous,
21 99.7%), and acetone (>99.9%) were purchased from Sigma-Aldrich. Tris(pentafluorophenyl)borane
22 (TPFPB, min. 97%) was purchased from Strem Chemicals, Inc. All the materials were stored in the
23 glovebox without any additional treatment.

24 **Characterization.** Scanning electron microscope (SEM, JEOL-7100F) was used to characterize the
25 morphology of the materials and element distribution. The samples were sputter-coated with

1 approximately 10 nm of gold before the analysis. FTIR characterization was conducted using Bruker
2 (Vertex 70 Hyperion 1000) within the range of 400-950 cm^{-1} and the resolution of the spectra was 4
3 cm^{-1} . Raman characterization was conducted using InVia (Renishaw) within the range of 100-2500
4 cm^{-1} and a laser source of 633 nm. X-ray photoelectron spectroscopy measurement was conducted
5 using PHI 5600. The ionic conductivity of PhNPs was measured by electrochemical impedance
6 spectroscopy method with a frequency ranges from 1 MHz to 0.1 Hz. The thermal conductivity was
7 measured by a thermal analyser (Hot Disk, TPS2500S).

8 **Preparation of PhNPs and T-PhNPs.** PVDF-HFP pellets were firstly dried in an oven at 100°C for
9 24 h and were dissolved in acetone at a concentration of 0.1 g mL^{-1} with rapid magnetic stirring for
10 about 8 h at 60°C. Next, 1M NaTFSI/PC solution with different mass ratios from 30 to 86 wt. % were
11 added to the PVDF-HFP solution to form a homogeneous mixture in an argon atmosphere. The
12 resulting mixture was then cast on a glass petri-dish and dried in a vacuum oven (10^{-3} Torr) at 60°C
13 for over 24 h to evaporate all the acetone solvent. Finally, the free-standing PhNP films were obtained.
14 For T-PhNPs, different amount of TPFPB was added to PhNP-86 mixtures at 60°C and then followed
15 the same evaporating procedures to obtain free-standing solid-state T-PhNP films. All the films were
16 stored in a glove box ($\text{O}_2 < 0.1$ ppm, and $\text{H}_2\text{O} < 0.1$ ppm) for future use.

17 **Fabrication of *i*-TE Device.** The as-fabricated *p*-type PhNP and *n*-type T-PhNP films were cut into
18 identical thin-rectangular shapes with a dimension of 6×1.5 mm^2 . The 13 pairs of the developed
19 thermocouple films were carefully transferred to the corresponding electrodes. Next was to make sure
20 the *p*-type and *n*-type films were electrically connected in series with the bridge gap between the hot
21 side and cool side larger than 2.0 mm. Then, the in-plane all-solid-state *i*-TE generator module
22 prototype can be ready for further test.

23 **MD calculation of thermal conductivity and ionic diffusion of PhNP systems.** All-atom molecular
24 dynamics (MD) simulations were used to predict thermal conductivity and ionic diffusion properties

1 of the solid-state *i*-TE material PVDF-HFP/NaTFSI/PC. The initial structures of PVDF-HFP chains,
2 NaTFSI, and PC molecules were generated using the freely available AVOGADRO software package⁴².
3 These structures were then geometrically optimized via the use of Generalized Amber Force field
4 (GAFF)³⁷. The structures were considered to optimize when the energy difference between two
5 successive interactions dropped below a threshold value (10^{-8} kJ mol⁻¹). The LigParGen web-based
6 service⁴³ is used to provide the OPLS force-field parameters (Supplementary II Fig. S7 and Table S1)
7 and partial atomic charges for the PVDF-HFP, NaTFSI, and PC molecules, which are placed together
8 in a cubic simulation box with a dimension of $25 \times 25 \times 25$ nm³ using PACKMOL⁴⁴. We adjusted the
9 number of PVDF-HFP, NaTFSI, and PC molecules so that the size of each system was kept consistent.
10 Periodic boundary conditions in all three dimensions were implemented. The cut-off distance for long-
11 range energy calculations was set to be 12 Å. The contribution of long-range interactions was
12 calculated via the particle-particle-particle-mesh (PPPM) solver⁴⁵. The Newton's equations of motion
13 were time-integrated with a time-step of 1 fs using Large-scale Atomic/Molecular Massively Parallel
14 Simulation (LAMMPS) package⁴⁶ developed by Sandia National Laboratories. The Visual Molecular
15 Dynamics (VMD)⁴⁷ was used to visualize the trajectories generated during simulations. Each sample
16 was equilibrated via the use of NPT simulations at 294 K and 1 atm over a period of 2 ns. Following
17 this, a further 5 ns simulation was performed in the NVT ensemble. We tracked a trajectory of 1000
18 frames that were generated every 1 ps. The whole trajectory was then used for calculating the RDF
19 and mean square displacement (Supplementary Fig. S8). In thermal transport simulations, the heat
20 source and heat sink were set as 320 K and 280 K, respectively, using Langevin thermostats
21 (Supplementary Fig. S9a). The system runs in the NVE ensemble for 1.5 ns to record heat flux and
22 temperature gradient across systems (Supplementary Fig. S9b-9c). The thermal conductivity of the
23 PhNP-30, -50, and -80 samples were calculated based on Fourier law using non-equilibrium molecular
24 dynamics simulation⁴⁸.

1 **Acknowledgments**

2 The authors are thankful for the financial support from the National Natural Science Foundation of
3 China (Grant No. 520006130, 51827807 and 51636002), China Postdoctoral Science Foundation
4 (Grant No. 2020M680024 and 2020M670321), Tsinghua-Foshan Innovation Special Fund
5 (2019THFS0125). We are grateful to Baris Demir from the University of Queensland for the useful
6 discussion about building molecular dynamics samples.

7 **Competing interest**

8 The authors declare no competing financial interest.

9 **Additional information**

10 Supplementary Information accompanies this paper at

11 **Data availability**

12

13 **References**

- 14 1 Bell, L. E. Cooling, heating, generating power, and recovering waste heat with thermoelectric
15 systems. *Science* **321**, 1457-1461, (2008).
- 16 2 Chu, S. & Majumdar, A. Opportunities and challenges for a sustainable energy future. *Nature*
17 **488**, 294-303, (2012).
- 18 3 Rahimi, M. *et al.* Emerging electrochemical and membrane-based systems to convert low-
19 grade heat to electricity. *Energy Environ. Sci.* **11**, 276-285, (2018).
- 20 4 Zhao, L. D. *et al.* Ultrahigh power factor and thermoelectric performance in hole-doped
21 single-crystal SnSe. *Science* **351**, 141-144, (2016).
- 22 5 Snyder, G. J. & Toberer, E. S. Complex thermoelectric materials. *Nat. Mater.* **7**, 105-114,
23 (2008).
- 24 6 Poudel, B. *et al.* High-thermoelectric performance of nanostructured bismuth antimony
25 telluride bulk alloys. *Science* **320**, 634-638, (2008).
- 26 7 Cheng, H. L., He, X., Fan, Z. & Ouyang, J. Y. Flexible quasi-solid state ionogels with
27 remarkable Seebeck coefficient and high thermoelectric properties. *Adv. Energy Mater.* **9**,
28 1901085, (2019).
- 29 8 Zhao, D. *et al.* Polymer gels with tunable ionic Seebeck coefficient for ultra-sensitive printed

1 thermopiles. *Nat. Commun.* **10**, 1093, (2019).

2 9 Akbar, Z. A., Jeon, J. W. & Jang, S. Y. Intrinsically self-healable, stretchable thermoelectric
3 materials with a large ionic Seebeck effect. *Energy Environ. Sci.* **13**, 2915-2923, (2020).

4 10 Kim, B., Hwang, J. U. & Kim, E. Chloride transport in conductive polymer films for an n-
5 type thermoelectric platform. *Energy Environ. Sci.* **13**, 859-867, (2020).

6 11 Han, C. G. *et al.* Giant thermopower of ionic gelatin near room temperature. *Science* **368**,
7 1091, (2020).

8 12 Li, T. *et al.* Cellulose ionic conductors with high differential thermal voltage for low-grade
9 heat harvesting. *Nat. Mater.* **18**, 608-613, (2019).

10 13 Kim, B. *et al.* Robust high thermoelectric harvesting under a self-humidifying bilayer of
11 metal organic framework and hydrogel layer. *Adv. Funct. Mater.* **29**, 1807549, (2019).

12 14 Wang, H. *et al.* Ionic thermoelectric figure of merit for charging of supercapacitors. *Adv.*
13 *Electron. Mater.* **3**, 1700013, (2017).

14 15 Zhao, D. *et al.* Ionic thermoelectric supercapacitors. *Energy Environ. Sci.* **9**, 1450-1457,
15 (2016).

16 16 Eastman, E. D. Theory of the Soret effect. *J. Am. Chem. Soc.* **50**, 283, (1928).

17 17 Bonetti, M., Nakamae, S., Roger, M. & Guenoun, P. Huge Seebeck coefficients in
18 nonaqueous electrolytes. *J. Chem. Phys.* **134**, 114513, (2011).

19 18 Fu, L., Joly, L. & Merabia, S. Giant thermoelectric response of nanofluidic systems driven by
20 water excess enthalpy. *Phys. Rev. Lett.* **123**, 138001, (2019).

21 19 Cheng, H. L. & Ouyang, J. Y. Ultrahigh thermoelectric power generation from both Ion
22 diffusion by temperature fluctuation and hole accumulation by temperature gradient. *Adv.*
23 *Energy Mater.* **10**, 2001633, (2020).

24 20 Fang, Y. L. *et al.* Stretchable and transparent ionogels with high thermoelectric properties.
25 *Adv. Funct. Mater.*, 2004699, (2020).

26 21 Jiao, F. *et al.* Ionic thermoelectric paper. *J. Mater. Chem. A* **5**, 16883-16888, (2017).

27 22 Li, S. & Zhang, Q. Ionic gelatin thermoelectric generators. *Joule* **4**, 1628-1629, (2020).

28 23 Chi, C. *et al.* Flexible solvent-free supercapacitors with high energy density enabled by
29 electrical-ionic hybrid polymer nanocomposites. *J. Mater. Chem. A* **7**, 16748-16760, (2019).

30 24 Kim, S. L., Lin, H. T. & Yu, C. Thermally chargeable solid-state supercapacitor. *Adv. Energy*
31 *Mater.* **6**, 160546, (2016).

32 25 Jia, H., Ju, Z., Tao, X., Yao, X. & Wang, Y. P-N conversion in a water-ionic liquid binary
33 system for nonredox thermocapacitive converters. *Langmuir* **33**, 7600-7605, (2017).

34 26 Duan, J. J. *et al.* P-N conversion in thermogalvanic cells induced by thermo-sensitive
35 nanogels for body heat harvesting. *Nano Energy* **57**, 473-479, (2019).

36 27 Das, S. & Ghosh, A. Charge carrier relaxation in different plasticized PEO/PVDF-HFP blend
37 solid polymer electrolytes. *J. Phys. Chem. B* **121**, 5422-5432, (2017).

- 1 28 Rahaman, M. H. A. *et al.* Effect of gamma irradiation on poly(vinylidene difluoride)-lithium
2 bis(oxalato) borate electrolyte. *Phys. Chem. Chem. Phys.* **16**, 11527-11537, (2014).
- 3 29 Lee, S. G., Ha, J. W., Sohn, E. H., Park, I. J. & Lee, S. B. Enhancement of polar crystalline
4 phase formation in transparent PVDF-CaF₂ composite films. *Appl. Surf. Sci.* **390**, 339-345,
5 (2016).
- 6 30 Ruan, L. X. *et al.* Properties and applications of the β phase poly(vinylidene fluoride).
7 *Polymers* **10**, 228, (2018).
- 8 31 Geng, C. X. *et al.* Influence of salt concentration on the properties of sodium-based
9 electrolytes. *Small Methods* **3**, 1800208, (2019).
- 10 32 Manning, G. S. Limiting laws and counterion condensation in polyelectrolyte solutions. 8.
11 Mixtures of counterions, species selectivity, and valence selectivity. *J. Phys. Chem.* **88**, 6654-
12 6661, (1984).
- 13 33 Chi, C. *et al.* Silicon-nanoforest-based solvent-free micro-supercapacitor with ultrahigh
14 spatial resolution via ic-compatible in-situ fabrication for on-chip energy storage. *J. Mater.*
15 *Chem. A* **8**, 22736-22744, (2020).
- 16 34 Yeon, S. H., Kim, K. S., Choi, S., Cha, J. H. & Lee, H. Characterization of PVdF(HFP) gel
17 electrolytes based on 1-(2-Hydroxyethyl)-3-methyl imidazolium ionic liquids. *J. Phys. Chem.*
18 *B* **109**, 17928-17935, (2005).
- 19 35 Bai, J. J., Lu, H. M., Cao, Y., Li, X. D. & Wang, J. R. A novel ionic liquid polymer electrolyte
20 for quasisolid state lithium air batteries. *Rsc Adv.* **7**, 30603, (2017).
- 21 36 Zhou, W. X. *et al.* Thermal conductivity of amorphous materials. *Adv. Funct. Mater.* **30**,
22 1903829, (2020).
- 23 37 An, M. *et al.* Predictions of thermo-mechanical properties of cross-linked polyacrylamide
24 hydrogels using molecular simulations. *Adv. Theor. Simul.* **2**, 1800153, (2019).
- 25 38 Zhao, L. D. *et al.* Ultralow thermal conductivity and high thermoelectric figure of merit in
26 SnSe crystals. *Nature* **508**, 373-377, (2014).
- 27 39 Ail, U. *et al.* Thermoelectric properties of polymeric mixed conductors. *Adv. Funct. Mater.*
28 **26**, 6288-6296, (2016).
- 29 40 Jiang, Q. L. *et al.* High thermoelectric performance in n-type perylene bisimide induced by
30 the Soret effect. *Adv. Mater.* **32**, 2002752, (2020).
- 31 41 Fondard, J. *et al.* SEI composition on hard carbon in Na-ion batteries after long cycling:
32 influence of salts (NaPF₆, NaTFSI) and additives (FEC, DMCF). *J. Electrochem. Soc.* **167**,
33 070526, (2020).
- 34 42 Hanwell, M. D. *et al.* Avogadro: an advanced semantic chemical editor, visualization, and
35 analysis platform. *J. Cheminformatics* **4**, 17, (2012).
- 36 43 Dodda, L. S., de Vaca, I. C., Tirado-Rives, J. & Jorgensen, W. L. LigParGen web server: an
37 automatic OPLS-AA parameter generator for organic ligands. *Nucleic Acids Res.* **45**, W331-

1 W336, (2017).

2 44 Martinez, L., Andrade, R., Birgin, E. G. & Martinez, J. M. PACKMOL: A package for
3 building initial configurations for molecular dynamics simulations. *J. Comput. Chem.* **30**,
4 2157-2164, (2009).

5 45 Demir, B., Chan, K. Y. & Searles, D. J. Structural electrolytes based on epoxy resins and
6 ionic liquids: a molecular-level investigation. *Macromolecules* **53**, 7635-7649, (2020).

7 46 Plimpton, S. Fast parallel algorithms for short-range molecular-dynamics. *J. Comput. Phys.*
8 **117**, 1-19, (1995).

9 47 Humphrey, W., Dalke, A. & Schulten, K. VMD: Visual molecular dynamics. *J. Mol. Graph.*
10 *Model.* **14**, 33-38, (1996).

11 48 An, M. *et al.* Mass difference and polarization lead to low thermal conductivity of graphene-
12 like carbon nitride (C₃N). *Carbon* **162**, 202-208, (2020).

13

Figures

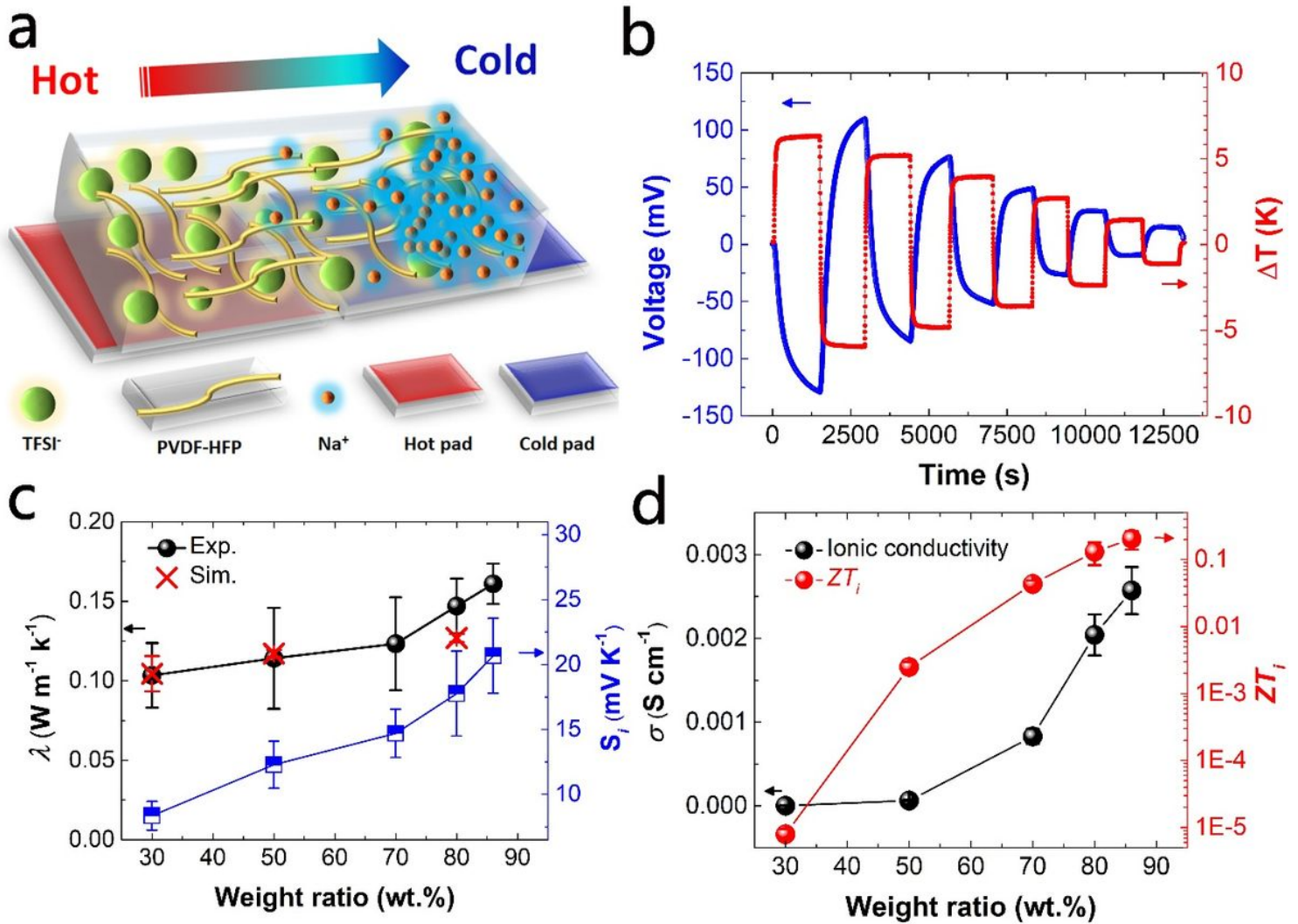


Figure 1

The thermoelectric performance of the p-type PhNP. (a) The diagrammatic illustration of the p-type (Na⁺ dominate thermodiffusion) PhNP i-TE materials. (b) The plot of the measured Vi-T curves of PhNP-86. (c) The measured thermopower, thermal conductivity together with simulation results of PhNPs. (d) The measured ionic conductivity and figure of merit ZT_i of each PhNPs.

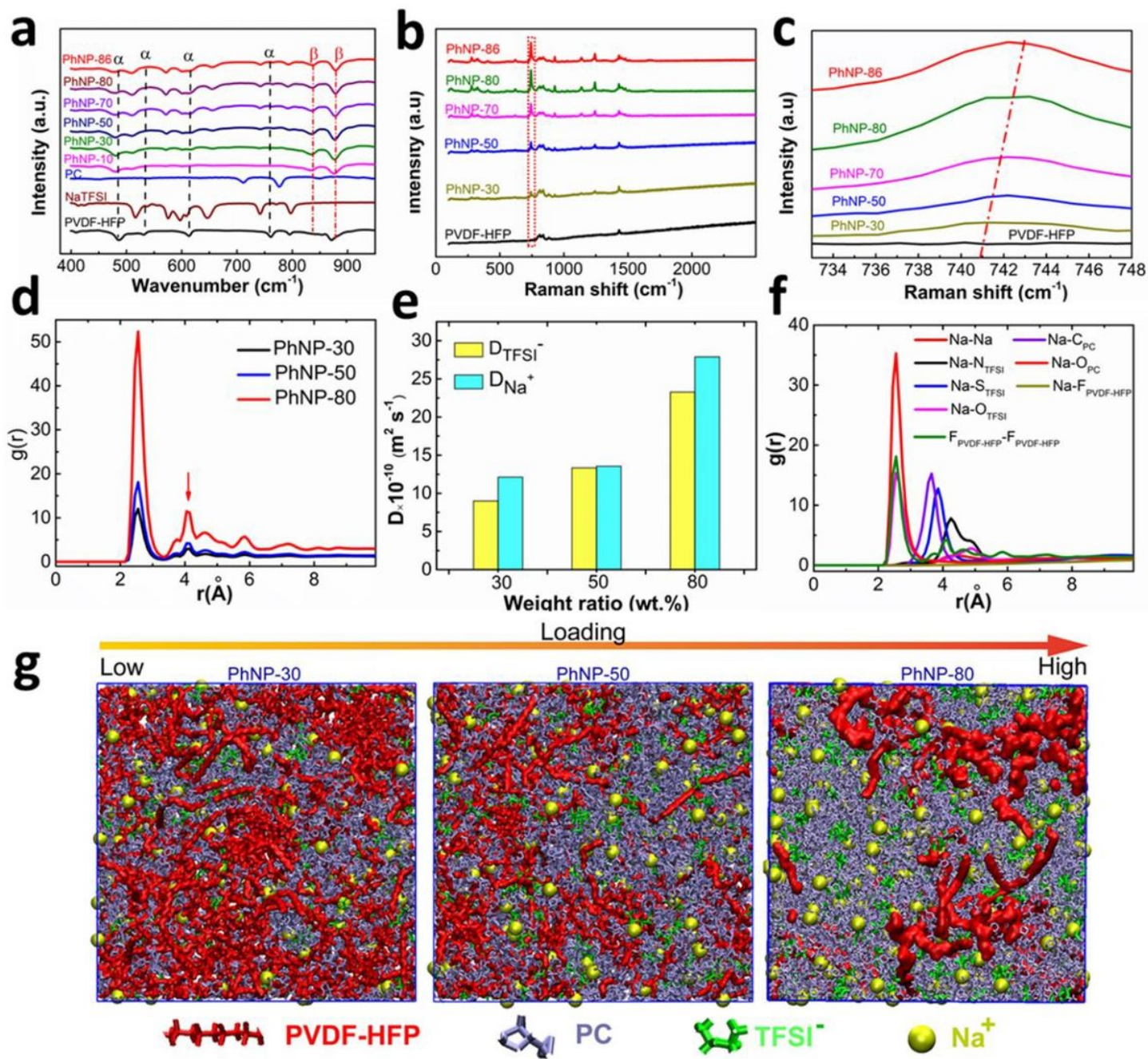


Figure 2

The structural characterization and atomic-level interaction in PhNPs. (a) FTIR spectra with a range of 400-950 cm^{-1} , (b) Raman spectra with a range of 100-2500 cm^{-1} , and (c) the enlarged view of Raman spectra with a range of 733-746 cm^{-1} of each PhNPs. (d) the calculated RDFs (e) and the diffusion coefficient of Na^+ and TFSI^- of the PhNP-30, -50 and -80 samples. (f) The RDF of each interaction among ions and PVDF-HFP of PhNP-50. (g) The snapshots of the MD simulation model.

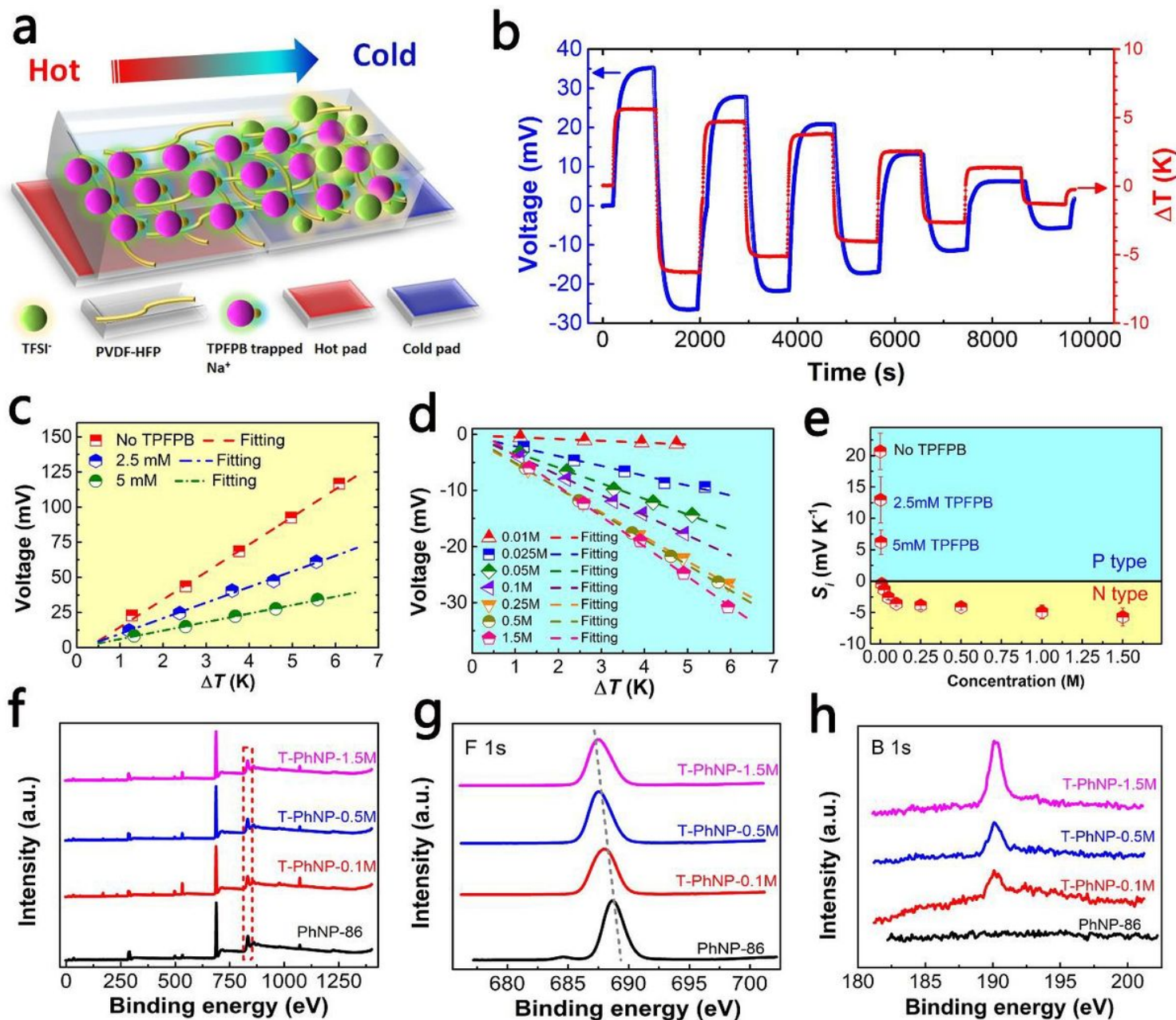


Figure 3

The conversion in p-type PhNP to n-type T-PhNP. (a) The schematic of ion transport of n-type (TFSI- dominate thermodiffusion) T-PhNP i-TE materials. (b) The measured thermoelectric voltage at a series of temperature difference of T-PhNP-1.5M. (c) and (d) The plot of ΔV_i - ΔT fitting curves and the calculated thermopower of each T-PhNPs. (f) XPS characterization of (g) F (1s) peak and (h) B (1s) peak of the T-PhNP with different amounts of TPFPB.

the as-fabricated i-TEG under 1.5 K. (f) Comparison of the thermopower range for the recent reported i-TE materials realizing p-n conversion^{8,25,26}.

Supplementary Files

This is a list of supplementary files associated with this preprint. Click to download.

- [SupportingInformation.pdf](#)